

Chandra monitoring of the very massive binary WR20a and the young massive cluster Westerlund 2

Y. Nazé^{1,*}, G. Rauw^{1,**}, and J. Manfroid^{1,***}

Institut d’Astrophysique et de Géophysique, Université de Liège, 17 allée du 6 août, Bât. B5C, 4000-Liège, Belgium
e-mail: naze@astro.ulg.ac.be

Received 15 October 2007 / Accepted 23 December 2007

ABSTRACT

Context. Westerlund 2 is a young and massive, obscured stellar cluster of our Galaxy. It harbors the most massive star with well-determined parameters, WR20a ($82 + 83 M_{\odot}$), a dozen very early O-type stars (O3–7), and a wealth of PMS stars. Although of clear significance, this star cluster has not been well-studied.

Aims. The high-energy properties of this cluster, especially those of its early-type stars are examined in detail. The variability of the X-ray sources is investigated.

Methods. A monitoring of the field was performed using three Chandra observations. This dataset probes daily as well as monthly to yearly timescales and provides the deepest X-ray view of the cluster to date.

Results. The two Wolf-Rayet stars WR20a (WN6ha+WN6ha) and WR20b (WN6ha) were analyzed in detail. They are both luminous and display hard spectra, but WR20b does not appear to vary. In contrast, WR20a, a known eclipsing, colliding-wind binary, brightens in the X-ray domain during eclipses, i.e. when the collision is seen face-on. This can be explained by the properties of the wind-wind collision zone, whose high density leads to a large absorbing column ($2 \times 10^{24} \text{ cm}^{-2}$).

All twelve O-type stars previously classified spectroscopically, two eclipsing binaries previously identified and nine newly-identified, O-type star candidates are detected in the high-energy domain; ten of those could be analyzed spectroscopically. Four are overluminous, but the others have typical L_X/L_{BOL} ratios, suggesting that several O-type objects are actually binaries. Variability at the $\sim 2\sigma$ level is detected for a majority of the sources, of unknown origin for single objects.

Faint, soft, diffuse emission pervades the entire field-of-view but no clear structure can be identified, even at the position of a blister proposed to correspond to the TeV source HESS J1023–575.

The X-ray properties of PMS objects, in particular the brightest flaring ones, are also investigated. They provided an additional argument in favor of a large distance (~ 8 kpc) for the cluster.

Key words. Galaxy: open clusters and associations: individual: Westerlund 2 – X-rays: stars – stars: individual: WR20a – stars: individual: WR20b

1. Introduction

1.1. The Westerlund 2 cluster

The young (1–2 Myr) stellar cluster Westerlund 2 lies in the H II region RCW49. It is an intense star forming region with numerous Pre Main Sequence (PMS) objects, as enlightened by recent Spitzer data (Churchwell et al. 2005, and references therein). The cluster also contains many early-type stars: at least two Wolf-Rayet stars, WR20a and WR20b (van der Hucht 2001), and twelve very hot O-stars with spectral types ranging from O3 to O6.5 (Rauw et al. 2007). In the IR and radio domains, these stars appear surrounded by two shells, one enclosing WR20a and the core of Westerlund 2, the other surrounding WR20b.

There are still many uncertainties about the properties and content of this cluster. For example, its distance is still a matter of intense debate. To cite only the most recent papers: Ascenso et al. (2007) and Tsujimoto et al. (2007) proposed a “low” value of 2–5 kpc, based on the X-ray and IR luminosities of PMS stars;

while Rauw et al. (2007) argue in favor of 8.0 ± 1.4 kpc, based on the spectrophotometric properties of the O-type star population and on the eclipsing characteristics of WR20a. Dame (2007) recently discussed the distance of the Westerlund 2 cluster on the basis of the CO emission of the giant molecular cloud MC8 (likely associated with the cluster) and the H I 21 cm absorptions along the line of sight towards Westerlund 2. This author found that the cluster must be located on the far side of the Carina spiral arm and inferred a kinematic distance of 6.0 ± 1.0 kpc in coarse agreement with the value of Rauw et al. (2007). An indirect argument can be added in favor of a “high” value, using the properties of the diffuse emission detected by Townsley et al. (2004). The latter authors found an X-ray luminosity of about $8\text{--}9 \times 10^{32} \text{ erg s}^{-1}$ (for an adopted distance of 2.3 kpc). Considering that the diffuse emission from massive-star forming regions typically amounts to $2\text{--}5 \times 10^{32} \text{ erg s}^{-1}$ per early-type star (Townsley et al. 2003, 2004), we would expect values of $3\text{--}7 \times 10^{33} \text{ erg s}^{-1}$ for a cluster containing at least 14 objects earlier than O7 (including the two Wolf-Rayet systems). This is compatible with the observed emission only if the distance is rather large (4–7 kpc rather than 2.3 kpc). In this paper, we will thus adopt 8 kpc as the distance to Westerlund 2.

* Postdoctoral Researcher FNRS.

** Research Associate FNRS.

*** Research Director FNRS.

1.2. X-ray properties

Studying the X-ray emission of young clusters provides crucial information, especially if the cluster is heavily obscured as in the case of Westerlund 2. PMS objects, mainly T Tauri stars, are more easily detected in the X-ray and IR domains, and their high-energy flares can be analyzed to determine their decay times, which are related to the physical size of the flaring region. In the high-mass range, the interacting colliding-wind binaries and young magnetic objects are more easily identified and their properties constrained in the X-ray domain. Furthermore, the large-scale interaction with the surrounding medium is better studied by the analysis of the diffuse X-ray emission.

The X-ray properties of Westerlund 2 have been studied in increasing detail through the years. The first detection of the cluster was made by the Einstein observatory: Goldwurm et al. (1987) reported the presence of one X-ray emitter at the position of RCW49, interpreted as unresolved sources or truly diffuse emission (from a supernova remnant or a wind-blown bubble). Using ROSAT, Belloni & Mereghetti (1994) detected possible diffuse emission and 24 point sources (7 of them being in our ACIS-I field-of-view), among which HD 90273, MSP18¹ and WR20a. The high X-ray luminosity of WR20a was suggested as possible evidence of an ongoing colliding-wind phenomenon. More recently, Townsley et al. (2004) and Tsujimoto et al. (2007) reported the results of a first Chandra observation. Thanks to its high spatial resolution, this facility is the first to resolve the individual sources in the core of Westerlund 2. More than 400 X-ray sources were identified by Tsujimoto et al. (2007), mostly PMS stars and a few early-type objects. Faint diffuse emission is also present; it extends to the southeast of the cluster and presents a soft spectrum plus a very faint hard tail (Townsley et al. 2004).

To investigate further the high-energy properties of Westerlund 2, especially those of its massive star population, we have obtained additional X-ray observations, which combine to provide the deepest X-ray view of the cluster. It enables us to study the variability of the X-ray sources on several timescales, short-term variations within one exposure and monthly to yearly changes between the datasets.

The paper is organized as follows. Section 2 presents the datasets and their data reduction. Sections 3 and 4 focus on the O-stars and WR-stars content, respectively. The search for a counterpart to the recently discovered TeV source and the presence of diffuse emission are discussed in Sect. 5, while Sect. 6 concentrates on the flaring sources. Finally, we conclude in Sect. 7.

2. Observations and data reduction

2.1. Journal of observations

Westerlund 2 was observed three times using the ACIS-I camera onboard the Chandra X-ray Observatory, first on 2003/08/23 for 38 ks (PI Garmire), then on 2006/09/05 and 2006/09/28 both for 50 ks (PI Rauw); for details see Table 1. The first dataset was taken in very faint mode, whereas the last two were taken in faint mode; in all cases, the frame time was the 3.2 s standard. For all three observations, the ACIS-I chips covered a similar field-of-view but the position angle was slightly different from one exposure to another.

¹ The MSP numbers come from the numbering scheme devised by Moffat et al. (1991).

Table 1. Journal of observations. Phases ϕ refer to the ephemeris of WR20a (Rauw et al. 2007).

Name	Start time	End time	ϕ
Obs 1	2003/08/23, 18:21:23	2003/08/24, 04:53:56	0.34–0.46
Obs 2	2006/09/05, 15:52:01	2006/09/06, 06:29:22	0.28–0.44
Obs 3	2006/09/28, 05:46:20	2006/09/28, 20:14:43	0.41–0.57

The datasets were downloaded from the CXC website² and we have followed their recommendations for the reduction and analysis of the data. As they had been processed by the latest version of the CIAO pipeline, we did not completely reprocess them.

2.2. Detailed data processing

Background flares were only detected for the first observation, and times with background count rates larger than 0.02 cts s^{-1} were therefore discarded. The astrometry was improved by comparing the position of the bright X-ray point sources WR20a and MSP18 with their counterparts in the NOMAD catalog³. Shifts in pixels of $(-0.19, 0.20)$, $(-0.10, 0.04)$, and $(0.14, 0.20)$ were applied using the CIAO task `wcs_UPDATE` to the first, second and third observation respectively. The event lists were then re-projected without randomization, first to apply this astrometric correction, then to match the X , Y coordinates from the last observation. A merged event list was created using the CIAO task `DMMERGE` (with `[subspace -expno]` to avoid an incorrect merging of the good time intervals). Source detection was performed on this merged event list using the CIAO wavelet algorithm. It was applied separately to 1024×1024 images of the whole field (pixel of $1.4''$), the central $8'$ (pixel of $0.5''$) and the core of the cluster (pixel of $0.25''$). The derived source positions were used to define source/background regions for use in estimating count rates or in extracting spectra.

Exposure maps were then calculated for each observation and each energy band, assuming a monochromatic source of energy 1 keV (total band, $0.3\text{--}10.$ keV), 0.7 keV (soft band S , $0.3\text{--}1.$ keV), 1.5 keV (medium band M , $1.\text{--}2.$ keV) and 3 keV (hard band H , $2.\text{--}10.$ keV), respectively. Merged exposure maps were obtained using the CIAO task `REPROJECT_IMAGE`. The resulting fluxed images (in units $\text{photons cm}^{-2} \text{s}^{-1} \text{px}^{-2}$) were used to derive background and exposure-corrected photon fluxes⁴. The merged data were also used to make the three-color images shown in Fig. 1.

Spectrum extraction was performed for each source detected with more than 100 counts in the merged event list. It was performed separately on each observation. As recommended by the CXC, we extracted the spectral response files with the tasks `MKACISRMF` and `MKARF` (the latter including a mask file when the considered source was close to a gap and affected by the spacecraft's dithering). When there were less than 100 counts per observation, the individual spectra were merged using the FTOOLS tasks `MATHPHA`, `ADDRMF`, `ADDARF`. Lightcurves were

² <http://cxc.harvard.edu/>

³ <http://cdsarc.u-strasbg.fr/viz-bin/Cat?I/297>

⁴ For a typical source with absorbed thermal emission ($N_{\text{avg West2}}^H = 10^{22} \text{ cm}^{-2}$ and $kT = 0.3 \text{ keV}$), a photon flux of $1 \text{ photon cm}^{-2} \text{s}^{-1}$ corresponds at the time of our observations to a count rate of 350 cts s^{-1} , an absorbed flux of $1.7 \times 10^{-9} \text{ erg cm}^{-2} \text{s}^{-1}$ and an unabsorbed flux of $5.7 \times 10^{-8} \text{ erg cm}^{-2} \text{s}^{-1}$.

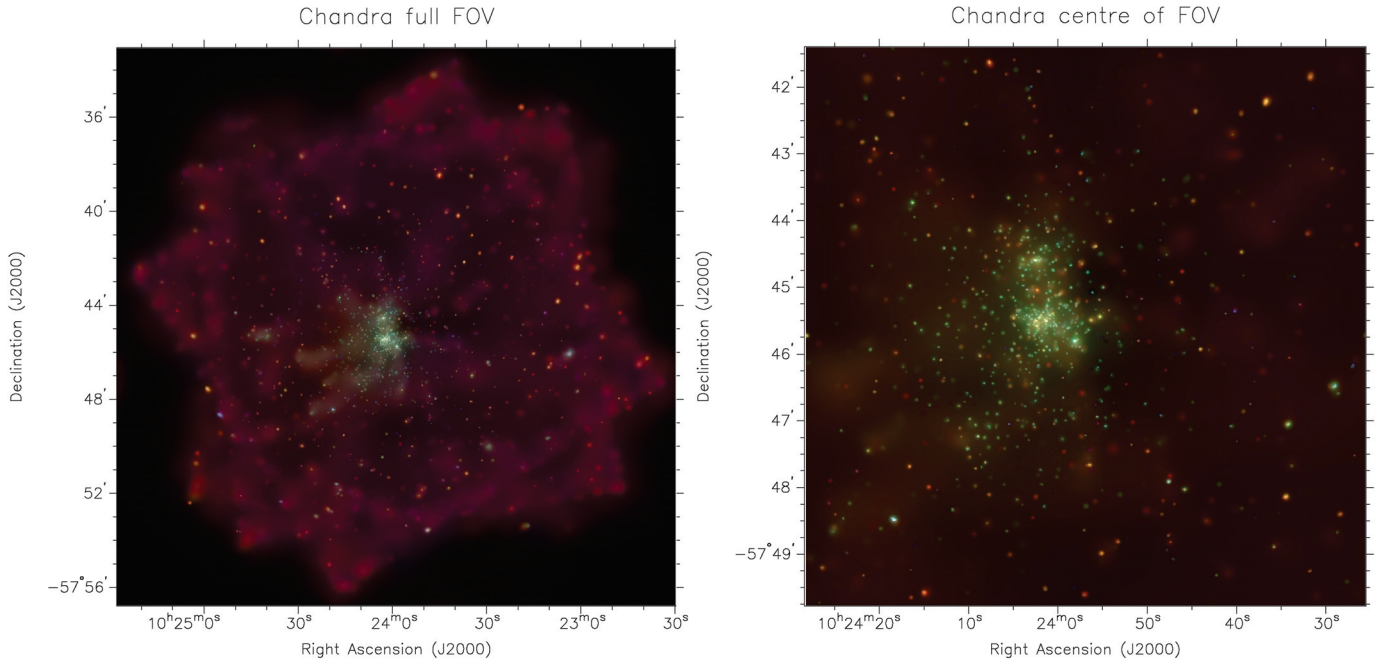


Fig. 1. Three-color images of Westerlund 2 in X-rays (**a**, left: full field; **b**, right: central 8' in the middle and **c**, below: core of the cluster). The red, green and blue colors correspond to soft (0.3–1 keV), medium (1–2 keV) and hard (2–10 keV) photon energies, respectively. The images were corrected by the exposure maps and adaptively smoothed prior to RGB combination.

extracted for the brightest sources using the CIAO task DMEXTRACT.

Throughout our analysis, we have used CIAO 3.4, CALDB 3.3.0.1 and Xspec 11.2.

3. O-type stars

3.1. Detection in the optical range

The first spectroscopic observations of the early-type population in Westerlund 2 revealed six O6-7 V: stars (Moffat et al. 1991). The presence of such “late” objects seemed incompatible with the presence of a very massive binary such as WR20a (see below). A new observing campaign was therefore undertaken, which led to a serious revision of the spectral types (Rauw et al. 2007): at least twelve O-type objects are present in Westerlund 2, with several of them displaying a very early type (O3–4). All twelve O-type stars catalogued by Rauw et al. (2007) are detected in the X-ray domain (see Fig. 2), but their characteristics differ significantly from one to the other (see below).

From the photometry of Rauw et al. (2007), we could also select O-star candidates: they have colors typical of early-type stars belonging to the cluster ($B - V$ between 1.3 and 1.6 mag, see Fig. 7 of that paper) and absolute magnitudes smaller than –3.9, a value typical of O9.5V stars (Martins et al. 2005). Some of these candidates are also definite X-ray emitters. The optical properties of this subgroup, composed of 9 objects, are presented in Table 2. Their color excess was derived from the observed color using an intrinsic color of –0.27, typical of O-type stars (Martins & Plez 2006). Then an estimation of their spectral type was made using their absolute V magnitude at an assumed distance of 8 kpc: they are late O-type stars, O7–O9.5. The relevant bolometric correction from Martins & Plez (2006) was then applied to find an estimate of their bolometric luminosities (Table 3).

We have added the O7 star HD 90273 to the list of O-type objects to analyze. Although this star is much more luminous

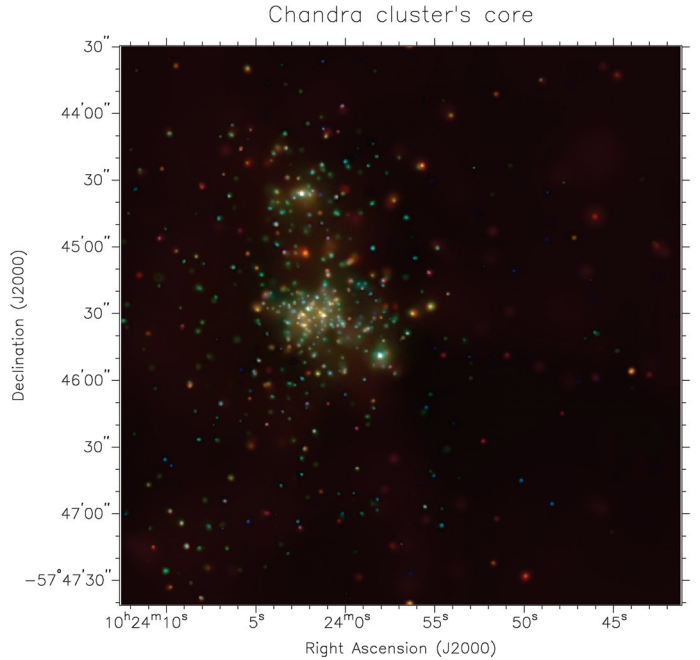


Fig. 1. continued.

and less absorbed than the stars of Westerlund 2, we have calculated its luminosity by assuming that it is an O7 supergiant at 8 kpc.

Spectral types, bolometric luminosities and absorbing columns (derived from the color excess using $N_{\text{int}}^{\text{H}} = 5.8 \times 10^{21} \times E(B - V)$, Bohlin et al. 1978) for the known O-type stars (from Rauw et al. 2007) and the candidates objects (calculated from the photometry as explained above) are shown in Table 3.

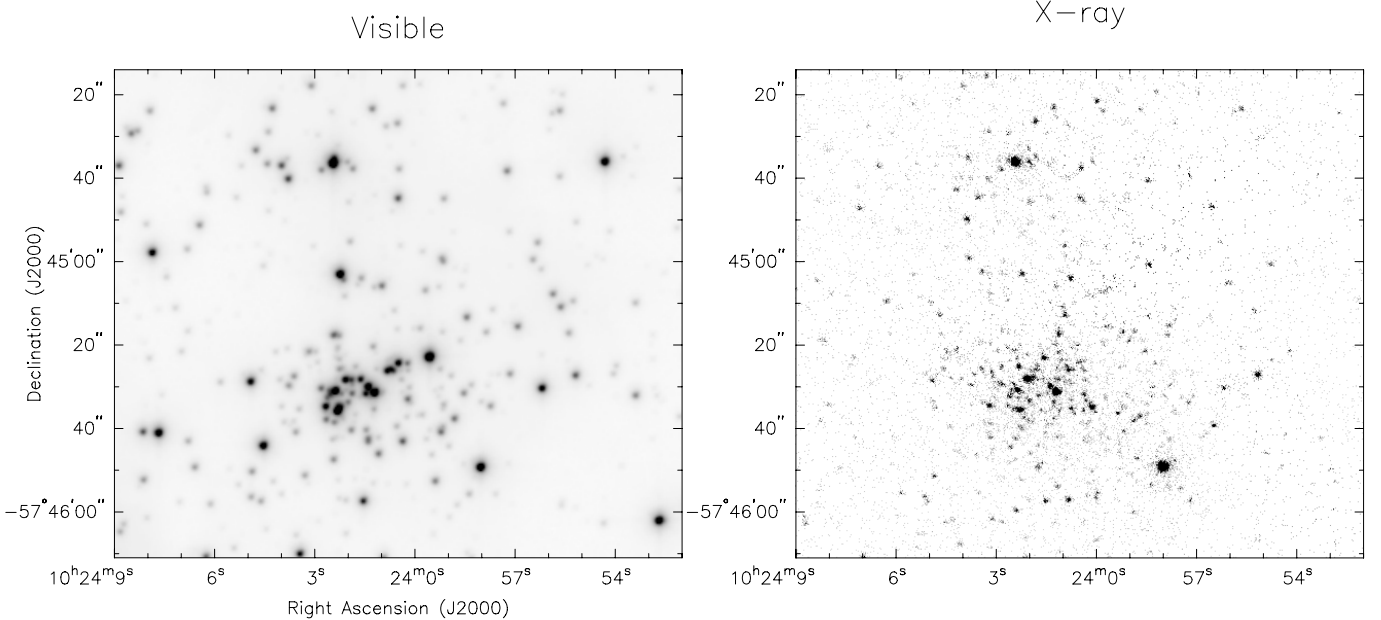


Fig. 2. The core of the Westerlund 2 cluster seen in visible (a), left) and X-rays (b), right). X-ray contours superimposed on the visible image (c), below; the X-ray data were adaptively smoothed).

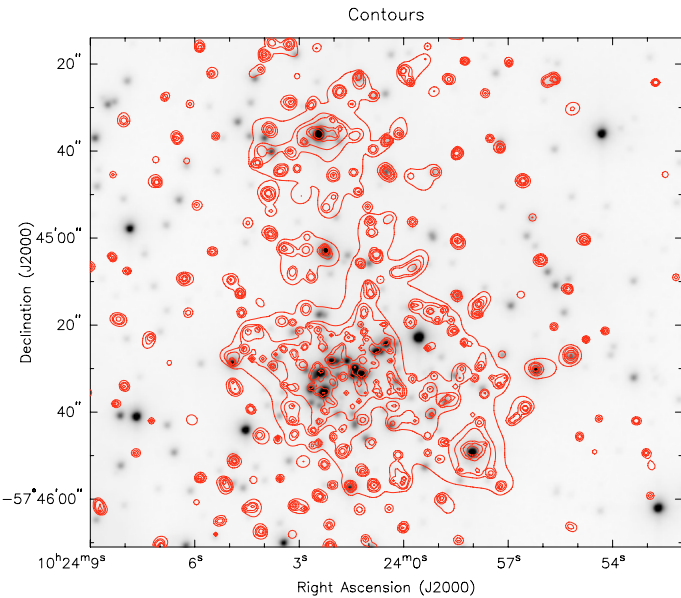


Fig. 2. continued.

Table 2. Properties of candidate late-O stars. The last two lines reproduces the data of two eclipsing binaries (from Rauw et al. 2007).

Name	RA, Dec (J2000)	$V \pm \sigma_V$	$B - V \pm \sigma_{B-V}$
MSP32	10:24:03.78, -57:44:39.8	15.355 ± 0.010	1.285 ± 0.014
MSP120	10:23:58.44, -57:45:13.0	16.211 ± 0.009	1.539 ± 0.016
MSP165	10:23:55.18, -57:45:26.9	15.604 ± 0.009	1.602 ± 0.013
MSP168	10:24:01.61, -57:45:27.8	14.829 ± 0.031	1.260 ± 0.039
MSP441	10:24:01.45, -57:45:31.3	14.918 ± 0.091	1.283 ± 0.138
Src 1	10:24:21.28, -57:47:27.6	14.671 ± 0.022	1.412 ± 0.025
Src 2	10:24:16.25, -57:43:43.8	14.914 ± 0.015	1.597 ± 0.017
Src 3	10:24:06.64, -57:47:15.8	16.473 ± 0.011	1.644 ± 0.019
Src 4	10:24:02.28, -57:45:35.3	13.302 ± 0.039	1.371 ± 0.059
MSP44	10:24:00.5, -57:44:45	15.67	1.25
MSP223	10:23:59.2, -57:45:40	15.75	1.50

3.2. X-ray properties

We first derived the photon rates using the fluxed images for the known O-type stars, the candidate late-O and the eclipsing binaries detected in the X-ray domain (see Table 3)⁵. The extraction region used for each star was a circle whose radius r , given in the second column of the table in Chandra pixels, is a compromise chosen to include most source photons while avoiding contamination from nearby sources; background regions were selected to be surrounding annuli or nearby circles devoid of sources. Errors on the photon rates and luminosities were estimated from the relative error on the net counts. Hardness ratios were calculated from the photon fluxes in the S , M , and H bands using $HR_1 = (M - S)/(M + S)$ and $HR_2 = (H - M)/(H + M)$. The X-ray luminosities in the 0.5–10. keV band were evaluated for a distance of 8 kpc using spectroscopic fits (only rough ones for the faintest objects) and were dereddened only for the interstellar column.

The brightest objects had sufficient counts to provide a detailed X-ray spectrum and they were thus also analyzed spectroscopically. The derived best-fit parameters are shown in Table 4. The second column provides the origin of the spectrum: Obs 1, 2, 3 or *Mgd* (for the case where a spectrum had insufficient counts to be analyzed individually). The fitted model has the form $wabs(N_{int}^H)^*wabs(N^H)^*mekal(kT)$ or $wabs(N_{int}^H)^*[wabs(N_1^H)^*mekal(kT_1) + wabs(N_2^H)^*mekal(kT_2)]$, with $wabs(N_{int}^H)$ fixed to the interstellar column (Rauw et al. 2007; Bohlin et al. 1978). In the table, quoted fluxes and luminosities are in the 0.5–10.0 keV energy range and the unabsorbed luminosities L_X^{unabs} are corrected only for the interstellar absorbing column. We note that lightcurves and spectra were extracted in the same regions as defined above. A plot of X-ray luminosity against bolometric luminosity if provided in Fig. 4.

⁵ Note that the values of the photon rates given in that table are raw, i.e. uncorrected for the encircled energy fraction, whereas the X-ray luminosity, derived from spectral fits, include that correction.

Table 3. Properties of the early-type stars in the optical and X-ray domains. Background- and exposure-corrected source fluxes (in 10^{-5} photons $\text{cm}^{-2} \text{s}^{-1}$) are estimated for each observation from the fluxed images in a region of radius r (in px) and for the 0.3–10. keV band. The last columns give the average hardness ratios and dereddened X-ray luminosity in 10^{32} erg s^{-1} and for the 0.5–10. keV energy band (see text for details). A colon (:) indicates an uncertain value.

Star	Sp. Type	$\log(L_{\text{bol}}/L_{\odot})$	$N_{\text{H}}^{\text{H}}/\text{10}^{22}$	r	Mean ph. flux	Obs 1	Obs 2	Obs 3	HR_1	HR_2	L_{X}	L_{unabs}	$\log(L_{\text{X}}/L_{\text{bol}})$
WR20a	WN6ha+WN6ha	6.28	1.13	4	11.87 ± 0.17	10.3 ± 0.4	11.2 ± 0.3	13.2 ± 0.3	0.64 ± 0.03	0.385 ± 0.012	51.7^a	-6.15	
WR20b	WN6ha	5.86	1.04	9	3.77 ± 0.09	3.69 ± 0.18	3.72 ± 0.15	3.88 ± 0.16	0.61 ± 0.08	0.656 ± 0.016	19.0^a	-6.16	
HD790273	O7I:	5.80:	0.22:	20	0.81 ± 0.06	1.03 ± 0.11	0.77 ± 0.09	0.66 ± 0.10	-0.83 ± 0.02	-0.79 ± 0.24	2.82^a	-6.93	
MSP18	O5.5V-III	5.89	0.88	3	6.92 ± 0.14	7.4 ± 0.4	6.4 ± 0.2	7.4 ± 0.2	0.38 ± 0.05	0.19 ± 0.02	35.8^a	-5.92	
MSP32 ^b	O9.5V:	4.61:	0.90:	3	0.025 ± 0.014	0.07 ± 0.04	0.006 ± 0.022	0.03 ± 0.02	-0.15 ± 0.50	-0.92 ± 1.38	0.15	-7.02	
MSP44 ^c	O9.5V:	4.44:	0.88:	4	0.23 ± 0.03	0.27 ± 0.08	0.23 ± 0.04	0.23 ± 0.05	1.	0.11 ± 0.12	0.53	-6.31	
MSP120 ^b	O9.5V:	4.58:	1.00:	4	0.050 ± 0.018	0.06 ± 0.05	0.08 ± 0.03	0.01 ± 0.02	-0.07 ± 0.47	-0.47 ± 0.59	0.41	-6.54	
MSP151	O7III	5.37	0.95	2	0.14 ± 0.02	0.12 ± 0.04	0.17 ± 0.03	0.13 ± 0.03	0.16 ± 0.29	-0.28 ± 0.16	0.57	-7.19	
MSP157	O5.5V	5.37	0.92	1.5	0.25 ± 0.02	0.35 ± 0.05	0.21 ± 0.04	0.20 ± 0.04	0.27 ± 0.20	-0.10 ± 0.10	1.16^a	-6.89	
MSP165 ^b	O7V:	5.09:	1.08:	4	0.52 ± 0.04	0.48 ± 0.06	0.63 ± 0.09	0.45 ± 0.08	0.57 ± 0.16	-0.49 ± 0.09	1.98^a	-6.37	
MSP167	O6III	5.14	0.98	2	2.05 ± 0.07	1.80 ± 0.12	2.25 ± 0.11	2.00 ± 0.13	0.57 ± 0.07	0.00 ± 0.04	8.85^a	-5.77	
MSP168 ^b	O8V:	4.90:	0.89:	2	0.079 ± 0.017	0.05 ± 0.03	0.08 ± 0.02	0.11 ± 0.02	-0.23 ± 0.27	-0.42 ± 0.25	0.41	-6.87	
MSP171	O5V	5.58	1.00	4	0.16 ± 0.03	0.13 ± 0.03	0.18 ± 0.04	0.13 ± 0.09	0.22 ± 0.27	-0.93 ± 0.35	1.09	-7.13	
MSP175	O5.5V-III	5.49	0.91	2	0.41 ± 0.03	0.34 ± 0.05	0.41 ± 0.05	0.45 ± 0.05	0.34 ± 0.14	-0.56 ± 0.08	1.78^a	-6.82	
MSP182	O4V-III	5.45	0.93	4	0.18 ± 0.03	0.20 ± 0.04	0.12 ± 0.04	0.22 ± 0.06	-0.24 ± 0.16	-0.76 ± 0.20	0.58	-7.27	
MSP183	O4V	6.07	1.03	2	0.70 ± 0.04	0.67 ± 0.07	0.60 ± 0.06	0.86 ± 0.09	0.09 ± 0.10	-0.44 ± 0.06	4.49^a	-7.00	
MSP188	O4V-III	5.93	0.96	2.5	3.43 ± 0.08	3.65 ± 0.17	3.41 ± 0.14	3.28 ± 0.14	0.23 ± 0.05	-0.10 ± 0.03	14.4^a	-6.35	
MSP199	O3V	5.61	0.97	2	0.11 ± 0.02	0.10 ± 0.03	0.10 ± 0.03	0.12 ± 0.03	0.50 ± 0.42	-0.56 ± 0.18	0.57	-7.44	
MSP203	O6V-III	5.84	0.95	2	0.57 ± 0.04	0.53 ± 0.07	0.49 ± 0.05	0.69 ± 0.06	0.12 ± 0.11	-0.35 ± 0.07	3.17^a	-6.92	
MSP223 ^c	O8.5V:	4.80:	1.00:	2	0.074 ± 0.015	0.04 ± 0.03	0.08 ± 0.02	0.08 ± 0.02	0.19 ± 0.41	0.18 ± 0.21	0.25	-6.98	
MSP263	O6.5V	5.45	1.09	4	0.20 ± 0.02	0.19 ± 0.04	0.24 ± 0.04	0.18 ± 0.03	0.30 ± 0.18	-0.47 ± 0.13	1.17^a	-6.96	
MSP441 ^b	O8V:	4.89:	0.90:	1.7	0.084 ± 0.015	0.09 ± 0.03	0.07 ± 0.02	0.10 ± 0.03	0.25 ± 0.40	-0.07 ± 0.19	0.30	-7.00	
Src 1 ^b	O6V:	5.31:	0.98:	5	0.071 ± 0.015	0.07 ± 0.03	0.10 ± 0.03	0.05 ± 0.02	0.15 ± 0.32	-0.91 ± 0.34	0.43	-7.26	
Src 2 ^b	O8.5III:	5.22:	1.08:	6	0.46 ± 0.03	0.54 ± 0.07	0.46 ± 0.05	0.63 ± 0.13	-0.45 ± 0.08	1.95^a	-6.52		
Src 3 ^b	O9.5V:	4.61:	1.10:	4	0.036 ± 0.010	0.05 ± 0.02	0.038 ± 0.017	>0.95	-0.40 ± 0.32	0.13	-7.08		
Src 4 ^b	O9.5I:	5.46:	0.95:	1.5	0.146 ± 0.018	0.06 ± 0.03	0.25 ± 0.04	0.10 ± 0.03	0.26 ± 0.12	0.57	-7.28		

^a From Table 4.

^b OB candidate.

^c Eclipsing binary.

Table 4. Best-fitting models and X-ray fluxes at Earth for the brightest early-type stars in Westerlund 2. For each parameter, the lower and upper limits of the 90% confidence interval (derived from the ERROR command under XSPEC) are noted as indices and exponents, respectively. The normalisation factors are defined as $10^{-14} \int n_e n_H dV / 4\pi D^2$, where D , n_e and n_H are respectively the distance to the source (8 kpc), the electron and proton density of the emitting plasma. Abundances were fixed to solar except for the WR stars (for more details, see text).

Star	Obs	$N_{\text{int}}^{\text{H}}$ 10^{22} cm^{-2}	N^{H} 10^{22} cm^{-2}	kT keV	Norm 10^{-3} cm^{-5}	χ^2_{ν} (d.o.f.)	f_X^{abs} $10^{-13} \text{ erg cm}^{-2} \text{ s}^{-1}$	L_X^{unabs} $10^{33} \text{ erg s}^{-1}$
WR20a	Obs 1	1.13	$1.53^{1.89}_{1.20}$	$0.87^{1.04}_{0.24}$	$1.57^{16.7}_{0.98}$	1.15 (33)	4.51	4.95
			$5.74^{14.6}_{1.89}$	$1.96^{6.38}_{0.87}$	$1.07^{10.7}_{0.29}$			
WR20a	Obs 2	1.13	$1.63^{1.92}_{1.40}$	$0.42^{0.50}_{0.32}$	$4.96^{10.9}_{3.04}$	1.26 (97)	4.10	4.88
			$5.48^{7.27}_{3.92}$	$1.30^{1.52}_{1.16}$	$2.61^{3.87}_{1.69}$			
WR20a	Obs 3	1.13	$1.93^{2.24}_{1.62}$	$0.35^{0.43}_{0.29}$	$9.60^{21.6}_{4.43}$	1.02 (119)	5.04	5.69
			$3.28^{4.53}_{2.40}$	$1.55^{1.75}_{1.39}$	$1.88^{2.53}_{1.44}$			
WR20b	Obs 1	1.04	$1.23^{1.88}_{0.67}$	$3.62^{8.05}_{2.44}$	$0.26^{0.38}_{0.18}$	1.24 (24)	2.06	1.88
WR20b	Obs 2	1.04	$2.18^{2.86}_{1.67}$	$2.47^{3.13}_{1.94}$	$0.41^{0.58}_{0.32}$	1.30 (35)	1.97	1.77
WR20b	Obs 3	1.04	$1.03^{1.48}_{0.67}$	$5.21^{6.72}_{3.70}$	$0.22^{0.28}_{0.18}$	1.97 (38)	2.29	2.05
MSP18	Obs 1	0.88	$0^{0.18}_{0.0}$	$3.24^{4.18}_{2.53}$	$0.31^{0.36}_{0.28}$	0.92 (18)	2.88	3.70
MSP18	Obs 2	0.88	$0^{0.13}_{0.0}$	$3.30^{3.64}_{2.81}$	$0.27^{0.30}_{0.26}$	1.10 (59)	2.54	3.24
MSP18	Obs 3	0.88	$0^{0.11}_{0.0}$	$3.04^{3.43}_{2.65}$	$0.32^{0.36}_{0.31}$	1.00 (56)	2.88	3.78
MSP167	Obs 1	0.98	$0.35^{0.88}_{0.0}$	$1.58^{2.27}_{1.07}$	$0.11^{0.19}_{0.08}$	1.02 (12)	0.52	0.77
MSP167	Obs 2	0.98	$0^{0.22}_{0.0}$	$2.32^{2.72}_{1.91}$	$0.10^{0.12}_{0.09}$	1.95 (21)	0.72	1.10
MSP167	Obs 3	0.98	$0.68^{1.15}_{0.0}$	$1.28^{2.32}_{0.91}$	$0.16^{0.28}_{0.09}$	0.95 (11)	0.56	0.78
MSP188	Obs 1	0.96	$0.45^{0.69}_{0.23}$	$1.22^{1.40}_{1.00}$	$0.24^{0.33}_{0.20}$	1.56 (26)	0.88	1.51
MSP188	Obs 2	0.96	$0.36^{0.52}_{0.0}$	$1.33^{1.86}_{1.20}$	$0.22^{0.26}_{0.16}$	0.73 (33)	0.88	1.49
MSP188	Obs 3	0.96	$0.70^{0.84}_{0.56}$	$0.97^{1.09}_{0.84}$	$0.30^{0.38}_{0.25}$	1.52 (30)	0.74	1.33
HD 90273	Mgd	0.22	$0.01^{0.38}_{0.0}$	$0.41^{0.52}_{0.22}$	$0.02^{0.17}_{0.0}$	0.88 (33)	0.16	0.28
MSP157	Mgd	0.92	$0^{0.51}_{0.0}$	$1.53^{1.92}_{1.08}$	$0.010^{0.018}_{0.0}$	0.97 (8)	0.057	0.12
MSP165	Mgd	1.08	$1.77^{2.48}_{1.29}$	$0.28^{0.38}_{0.20}$	$1.66^{13.2}_{0.0}$	0.59 (10)	0.088	0.20
MSP175	Mgd	0.91	$1.31^{1.88}_{1.18}$	$0.21^{0.28}_{0.14}$	$2.25^{59.8}_{0.0}$	1.20 (15)	0.057	0.18
MSP183	Mgd	1.03	$0.56^{0.85}_{0.36}$	$0.63^{0.82}_{0.45}$	$0.10^{0.25}_{0.0}$	0.94 (20)	0.14	0.45
MSP203	Mgd	0.95	$0.19^{0.47}_{0.0}$	$0.99^{1.14}_{0.74}$	$0.03^{0.05}_{0.02}$	1.09 (21)	0.11	0.32
MSP263	Mgd	1.09	$1.09^{1.65}_{0.62}$	$0.31^{0.53}_{0.18}$	$0.25^{5.98}_{0.0}$	0.89 (7)	0.034	0.12
Src 2	Mgd	1.08	$1.42^{1.71}_{0.71}$	$0.39^{0.68}_{0.33}$	$0.40^{0.77}_{0.0}$	1.20 (16)	0.088	0.19

3.2.1. Bright X-ray emitters

Since the first detection of massive stars in the X-ray domain, it has been known that their X-ray luminosity scales with their bolometric luminosity following $L_X \sim 10^{-7} L_{\text{BOL}}$ (the so-called “canonical” relation, see e.g. Berghöfer et al. 1997). Recent results have shown that this relation is rather tight for homogeneous groups of stars (NGC 6231 see Sana et al. 2006, and Carina OB1 see Antokhin et al. 2007). Outliers are generally peculiar objects, i.e. magnetic stars or colliding-wind binaries. In Westerlund 2, four of the bright sources clearly lie above the “canonical” relation with L_X/L_{BOL} ratios larger than -6.4 . The brightest one, MSP18, presents a $\log(L_X/L_{\text{BOL}})$ of -5.9 (to be compared with the -6.9 of Sana et al. 2006) and a high temperature ($kT > 1$ keV). No significant variations in intensity are evident in the short-term lightcurves of MSP18 (see Fig. 3). The luminosity of MSP18 has however dropped by 15% in the second observation (Table 3). Due to the limited signal-to-noise ratio, it is difficult to judge which parameter has changed from one observation to another (flux, temperature, or absorbing column), but the high luminosity, the hardness of the spectrum, and the variability suggest that the star is a colliding-wind binary or

a magnetic object. Note that binarity is also suggested by the position of the star in the optical color-magnitude diagram of Westerlund 2 (Rauw et al. 2007). MSP167 and 188 present similar properties, with $\log(L_X/L_{\text{BOL}})$ of -5.8 and -6.3 , respectively, and a variability at the 2σ level between pointings. Although no large variation is seen for the full band short-term lightcurves (Fig. 3), MSP188 exhibits some peculiar 2σ change (an increase followed by a decrease) in its soft X-ray flux during the last observation. MSP165 also displays a rather large $\log(L_X/L_{\text{BOL}})$ of -6.4 and some variability (at the 2σ level, the source is 30% more luminous in the second observation), but the source is overall quite soft. All of these sources should be considered as potential binaries, and deserve a spectroscopic monitoring in the visible domain which is currently underway.

The other bright objects have more typical $\log(L_X/L_{\text{BOL}})$, with values between -6.5 and -7.3 . Among these, MSP157 and 203 display unusually high temperatures. Some of these objects also exhibit $2-3\sigma$ variations: HD 90273 is 36% less luminous in the last observation, MSP183 and 203 are 35% more luminous in the last observation, the flux of MSP157 almost doubles in the first observation, whereas that of Src2 increases by 35%. If these

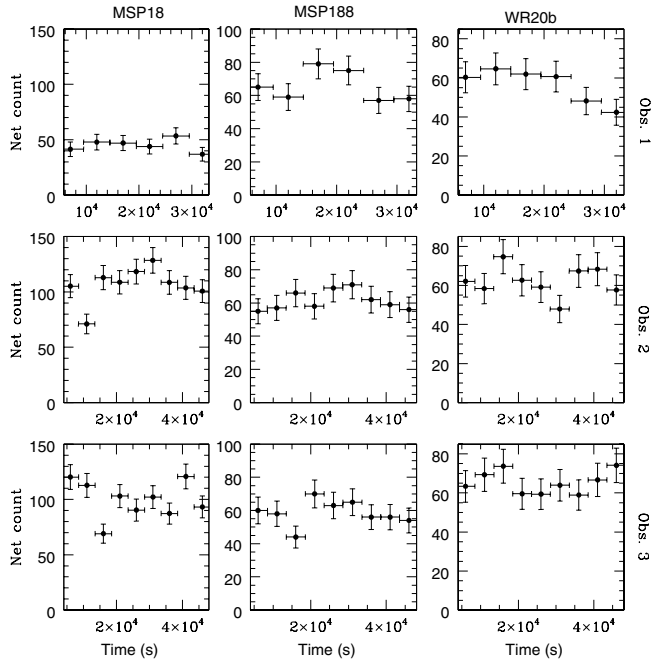


Fig. 3. Full band background-corrected lightcurves in units of counts per 5 ks bin for the three Chandra observations (*earliest at the top, latest at the bottom*). Data from MSP18 are shown in the *left panel*, those of MSP188 in the *middle one* and those of WR20b in the *right one*. Note that the first and last bins, when affected by incompleteness, were discarded and that the first observation of MSP18 was affected by the spacecraft’s dithering (thereby explaining the lower number of recorded counts).

stars are really single, as their modest luminosity suggests, it is difficult to determine the cause of their variability.

3.2.2. Faint X-ray sources

The faintest X-ray emitters of this sample (13 out of 26) did not have sufficient counts for a detailed spectroscopic analysis (less than 100 counts in total). We must therefore rely only on their photon fluxes and rough “color” properties. In this category, we find four O-type stars classified by Rauw et al. (2007): from their bolometric luminosity and extinction, we would have expected at least 300 counts for each of these but we detect less than 100 counts. This is especially surprising for MSP199, an O3-4 star that should be at least as luminous as the neighbouring MSP183 (also O3-4) and certainly more luminous than the neighbouring MSP203, an O6 object. However, Fig. 2 clearly shows that it is not the case. Only a few of these stars are found significantly variable at the 2σ level: MSP182 is 40% less luminous in the second observation, MSP32 is nearly undetected and Src4 is 3–4 times more luminous in that same exposure; MSP168 is 50% less luminous in the first observation, while this happens for Src1 in the last one. Overall, their L_X/L_{BOL} follows the “canonical” relation (Fig. 4), but some of them display large HRs (MSP223, Src 4, MSP44).

In conclusion, most O-type stars appear to follow the $L_X - L_{BOL}$ relation derived for the somewhat later O-type stars of NGC 6231. The larger scatter for Westerlund 2 can largely be explained by the fainter X-ray fluxes and the poorer knowledge of their properties, notably multiplicity, compared e.g. to NGC 6231 (Sana et al. 2006). The situation appears definitely

more complicated than the faint+soft vs. bright+hard dichotomy suggested by Tsujimoto et al. (2007, see also Fig. 4).

4. Wolf-Rayet stars

4.1. WR20a

In 2002, WR20a was serendipitously found to be a binary with $P = 3.7$ d and $e = 0$. Follow-up analyses revealed the system to be the most massive binary known with accurately determined masses: it consists of two very similar components of $82\text{--}83 M_\odot$ each (Rauw et al. 2005, and references therein). This exceptional object also harbors a wind-wind collision that triggers line profile variability in the visible domain (Rauw et al. 2005). The two components have types WN6ha, but they are only “Wolf-Rayet stars in disguise”, i.e. they are likely core-hydrogen burning stars with high mass-loss rates, only slightly evolved off the main sequence.

4.1.1. X-ray spectrum

In Rauw et al. (2005), the wind composition of WR20a was analyzed: the helium abundance was found to be consistent with solar, but the nitrogen abundance is measured to be six times solar and the carbon abundance approximately equal to or less than 4% solar. We include these chemical peculiarities in the spectral fitting, and freeze the abundances of other elements at solar values. Two-temperature components were necessary to obtain good fits (Table 4). We note that the low-temperature component appears to vary the most between observations.

The X-ray spectrum of WR20a appears overall rather hard. This is partially due to the absorption by the large interstellar column density, but reflects also the intrinsic hardness of the spectrum. Indeed, our two-temperature fits of the ACIS spectra of this source indicate temperatures around 1.3–2.0 keV for the hotter component. We emphasize that plasma at temperatures that high is usually not found in the winds of single early-type stars, thus suggesting that a significant part of the X-ray emission of WR 20a arises in the wind interaction region. Assuming that the emission arises from a radiatively-cooling, shock-heated plasma, we find that pre-shock velocities of about 1000 km s^{-1} are required to account for this hot plasma. This is twice the value of the on-axis pre-shock velocity of the wind-wind interaction that we estimated from a simple β velocity law (Rauw et al. 2005). This probably indicates that such a simple approximation of the pre-shock wind velocity law is not appropriate in an interacting-wind, close binary system such as WR20a. It might also mean that the contribution from the off-axis collision, which occurs at higher speed, is not negligible. In what follows we shall thus assume that the pre-shock velocity amounts to 1000 km s^{-1} .

4.1.2. X-ray lightcurve

The three Chandra exposures were taken around the secondary eclipse: Obs 1 samples the descending branch⁶, Obs 2 corresponds to phases slightly before and at the beginning of the eclipse, while Obs 3 covers the entire eclipse (Fig. 5). A first important conclusion from the *Chandra* light curve of WR20a is the lack of an X-ray eclipse. This result can only be explained if the X-ray emitting region is large. The absence of

⁶ Note that we need to be rather cautious about the results from the first observation, since during this exposure WR20a moved in and out of CCD2 due to the spacecraft’s dithering.

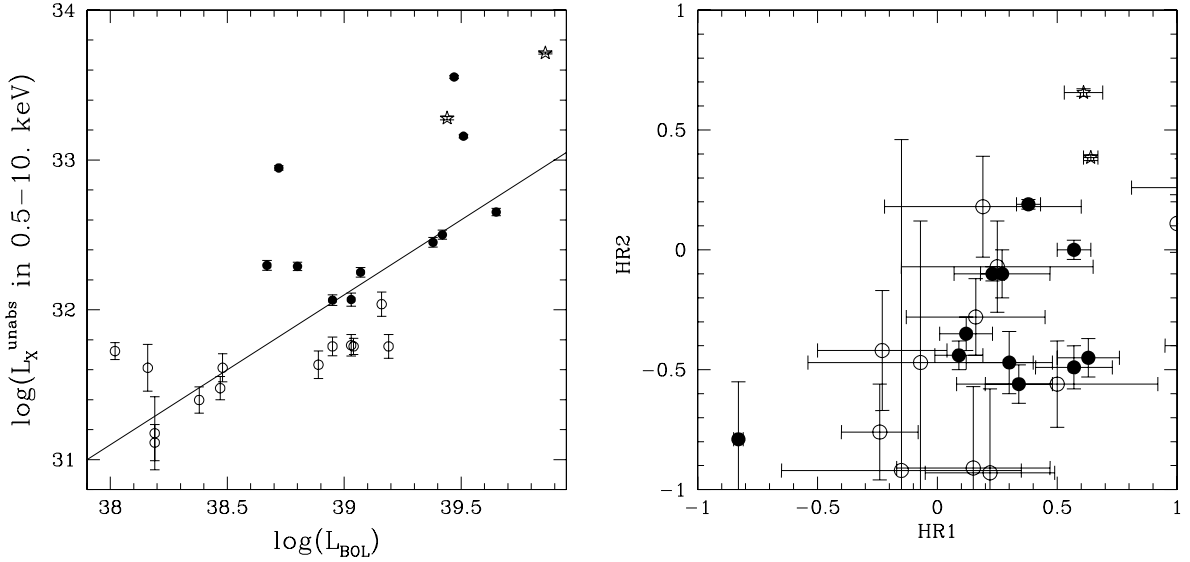


Fig. 4. *Left:* X-ray luminosity vs. bolometric luminosity. The solid line corresponds to the canonical relation of Sana et al. (2006); the stars represents the Wolf-Rayet objects, the filled circles the brightest O-type stars (see Table 4) and the open circles the faintest ones (see Table 3). *Right:* hardness ratios, symbols as in the left panel.

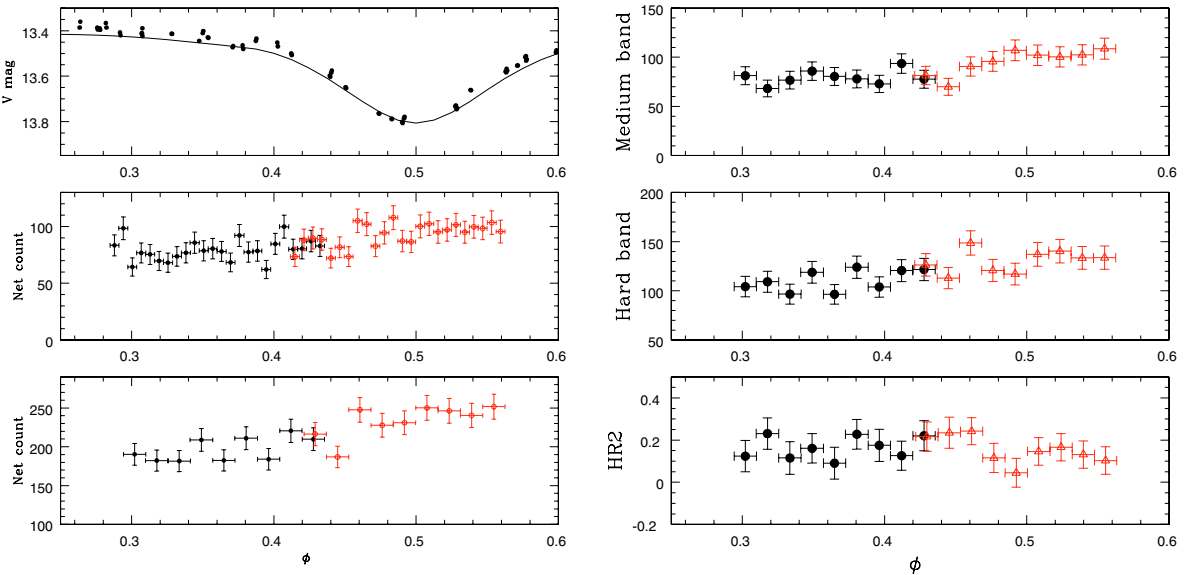


Fig. 5. *Left:* visible lightcurve of WR20a (*top figure*), X-ray lightcurves for the full energy band with bins of 2 ks (*middle figure*) and 5 ks (*bottom figure*). *Right:* lightcurve in the medium (M , *top*) and hard (H , *middle*) bands, together with evolution of the hardness ratio $HR_2 = (H - M)/(H + M)$ with phase (*bottom*), all shown in 5 ks bins. The X-ray data from the second observation are shown in solid black circles and those from the third one in open red triangles; incomplete bins were discarded. The uncertainty on the phase σ_ϕ is about 0.01, taking into account the uncertainty on the period and the time elapsed since our optical observations (~ 700 d, Rauw et al. 2007).

strong variations could be explained if the X-ray emission of WR 20a were produced in the individual winds, i.e. without a strong contribution from the wind interaction. However, there are two arguments against this assumption: first the rather high plasma temperature (see above) and second the X-ray luminosity that corresponds to an L_X/L_{bol} ratio well in excess of that of single early-type (actually O-type) stars. Such properties are indeed more typical of colliding-wind binaries (either O+O or O+WR). In the framework of a model where the X-ray emission arises midway between the stars as a result of a wind interaction, the absence of an eclipse sets stringent constraints on the

minimum size of the X-ray emitting region. For an orbital inclination of 74.5° (see Rauw et al. 2007, and references therein), we find that the lack of an occultation implies a strict minimum radius of the emitting region of $12 R_\odot$.

The lightcurve not only reveals the absence of eclipse, it also indicates a brightening of the emission near conjunction phase, i.e. when the collision region is seen face-on. More precisely, on the fluxed images, WR20a appears 20–30% more luminous in the last observation while the photon fluxes in the first two exposures are compatible within $2-3\sigma$ (Table 3). During each exposure, increasing trends are detected, but individual bins are

generally within one or two sigma of a constant value. The last two observations, during which WR20a was unaffected by dithering, follow each other in phase, and the behaviour of WR20a can thus be more easily quantified when the lightcurves are folded in phase (Fig. 5). At the beginning, WR20a presented about 175 counts per 5 ks-bin, while at the end it reached 250 counts per 5 ks-bin. If we compare the lightcurve in the hard and medium bands⁷ (see Fig. 5), the increase appears slightly larger in the latter, thereby leading to a slightly smaller hardness ratio in the last observation. The binary is thus significantly X-ray brighter and somewhat softer during the photometric eclipse.

4.1.3. Interpretation

A possible explanation for this puzzling result could come from the orbital modulation of the absorption in the dense wind interaction itself. Since the winds of the two components of WR 20a most likely have the same strength, the “stagnation” point, where the hottest plasma and hence the hardest X-ray emission is expected, should be located roughly at the centre of mass of the binary. The column density to the centre of mass is determined mostly by the density of the postshock material and by the thickness of the postshock region along the line of sight. Near quadrature phases, the column density along the line of sight is largest because the line of sight crosses the material close to the centre of mass where the density is largest.

Antokhin et al. (2004) provided a semi-analytical model for a radiative wind interaction zone⁸. These authors propose to calculate the cooling length l_0 as $l_0/r \approx 0.01 v^5 r \sin^3 \theta / \dot{M}$ where r is the distance between the centre of the star and the stagnation point in R_\odot , v is the local wind velocity in 10^3 km s^{-1} , θ is the angle between the tangent to the interaction front and the local wind direction and \dot{M} is the mass-loss rate in $10^{-6} M_\odot \text{ yr}^{-1}$. In the part of the interaction region around the binary axis, that is of most relevance for X-ray emission, the deflection due to the orbital motion is relatively small and hence $\theta = \pi/2$. For WR 20a, we further adopt $r = a/2 = 27 R_\odot$, $v = 1000 \text{ km s}^{-1}$ and $\dot{M} = 8.5 \times 10^{-6} M_\odot \text{ yr}^{-1}$ (see Rauw et al. 2005, and Sect. 4.1.1. for v). This then leads to $l_0 \approx 0.86 R_\odot$. Due to the steep temperature dependence of the radiative cooling, the width of the postshock cooling layer is of order $2 l_0/7$ (Antokhin et al. 2004), which then yields about $0.25 R_\odot$. Antokhin et al. (2004) further showed that the surface density of the shock region on the binary axis σ_0 should be equal to $\sigma_0 = \dot{M}/4\pi v a$. For WR 20a, this number amounts to about 0.11 g cm^{-2} , implying a mean density in the postshock cooling layer of about $6.7 \times 10^{-12} \text{ g cm}^{-3}$. If we assume that the wind interaction region within a radius of $12 R_\odot$ around the binary axis is delimited by two parallel planar shocks, integrating the density along the direction perpendicular to the binary axis (using equation [32] of Antokhin et al. 2004) and assuming the same chemical composition as Rauw et al. (2005) yields a (highly ionized) hydrogen column density N^H of order $2 \times 10^{24} \text{ cm}^{-2}$. This extremely large value⁹ over (probably) only a limited fraction of the interaction region shows that the absorption of the X-ray emission by the material of the interaction region must indeed be quite substantial around

quadrature phases. Of course, this large value of the column density only applies to a single point (the stagnation point on the binary axis). Since the X-ray emission arises over an extended part of the wind interaction region, the actual (observable) absorption will be lower. In addition, in a highly radiative wind interaction, various kinds of instabilities are expected to affect the shape of the interaction region (Stevens et al. 1992), making it deviate significantly from a simple planar region. The latter effect will reduce the peak value of the column density towards the stagnation point, but will also broaden the episode of high absorption around quadrature phases.

4.2. WR20b

Little is known about WR20b. van der Hucht (2001) assigned it a type WN6ha, whereas Shara et al. (1991) prefer WN7. As types and ages are similar for both Wolf-Rayet stars, we have used the same chemical composition for the spectral fits (Table 4) as well as the same intrinsic color and bolometric correction as for WR20a. Combined with our photometry ($V = 13.51 \pm 0.02$, $B = 14.98 \pm 0.02$), this leads to a bolometric luminosity of about $7.3 \times 10^5 L_\odot$, i.e. slightly fainter than the faintest component of WR20a (Rauw et al. 2007).

The photon rates and hardness ratio of WR20b are presented in Table 3 while its spectral properties for each observation can be found in Table 4. Overall, the system is 37–38% less luminous than WR20a both in the visible and in X-rays. The spectral fits reveal a large extinction, typical of Wolf-Rayet objects, but also a high temperature. The hardness ratio is also large, even larger than for WR20a (Fig. 4). Such properties are only expected for interacting binaries. However, the X-ray flux appears rather constant on both short and long timescales (Fig. 3 and Table 3), suggesting that the star is single. This contradictory result is important in the context of the current debate about the level of intrinsic X-ray emission from WN stars: while some apparently single WN stars, such as WR40 (Gosset et al. 2005), remain undetected in X-rays, other objects, e.g. WR6 and 110 (Skinner et al. 2002), clearly emit X-rays. WR20b seems to belong to the latter category. An optical monitoring is under way to better constrain the nature of WR20b.

5. HESS J1023–575 and the diffuse emission

Aharonian et al. (2007) recently reported the discovery of TeV high-energy γ -ray emission in the vicinity of Westerlund 2 with the HESS Cherenkov telescope array. This emission appears extended with a Gaussian fit yielding $\sigma = (0.18 \pm 0.02)^\circ$, equivalent to a diameter of 28 pc for a distance of 8 kpc. The source center lies 40s (or 5.5') west of WR 20a. Therefore, it is unlikely to be associated with WR 20a alone, especially since the photon-photon absorptions in the wind interaction zone of the colliding-wind binary are likely to be extremely severe, preventing TeV emission from escaping from the inner regions of the wind interaction zone of WR 20a. The size of the source is more typical of a wind-blown bubble. Aharonian et al. (2007) accordingly propose the TeV source to be associated with a blister-like structure detected in the radio range west of the cluster (Whiteoak & Uchida 1997).

To explain the TeV emission, Bednarek (2007) proposed a hybrid model where both leptons and hadrons contribute to the γ -ray emission from young, open clusters. In this model, the leptons are responsible for X-ray and GeV γ -rays through synchrotron and inverse Compton radiation, whilst the hadrons produce the TeV γ -ray emission through π^0 pion decay. The

⁷ Since WR20a is heavily absorbed, there are insufficient counts to produce a lightcurve in the soft band.

⁸ The χ cooling parameter of Stevens et al. (1992) amounts to about 0.02 for WR20a.

⁹ Note that due to the steep dependence on the pre-shock velocity, adopting $v = 500 \text{ km s}^{-1}$ would imply a column density about 60 times larger, and a pre-shock velocity of 1500 km s^{-1} a value ten times lower.

electrons and the hadrons would be accelerated at the shocks resulting from the interaction of the stellar winds of the massive stars with the surrounding matter. Whilst the relativistic electrons lose their energy inside the lower density cavity created by the winds of the massive stars, the relativistic protons travel over larger distances and will only lose their energy when interacting with the dense ambient giant molecular cloud. Hence the TeV emission produced by these particles should be more extended than the X-ray and GeV emission.

An alternative explanation has been proposed by [Anchordoqui et al. \(2007\)](#) who suggest that the TeV emission seen towards Westerlund 2 could be the result of Lorentz-boosted MeV γ -rays emitted in the de-excitation of daughter nuclei produced by the photo-disintegration of PeV cosmic-ray nuclei in the radiation field of the early-type stars inside the cluster core.

In some of the scenarios discussed above, the TeV emission is expected to have an extended counterpart in the X-ray domain. However, in the *Chandra* observation, the diffuse emission pervades most of the field and appears rather featureless: our X-ray data provide no clear indication of a blister-like structure (Fig. 1). The brightest emission is to be found to the southeast of the cluster, not towards the radio blister, and no bright X-ray point source is detected in the close vicinity of HESS J1023–575. Moreover, the X-ray spectrum of the diffuse emission appears mainly thermal although a faint, hard component might (or might not) be non-thermal ([Townsley et al. 2004](#)).

6. Variable X-ray sources

A photometric analysis was carried out on the 0.3–10 keV fluxed images of each observation using the standard procedures for aperture photometry available using IRAF. The positions of the sources have been derived from the merged data in order to increase the signal-to-noise ratio. Apertures with radii between 1.5'' to 5'' were used. The relative errors were estimated from the photon statistics derived from fluxes in the uncorrected images.

To identify flaring sources, we have compared the photon rates of each source in the three observations. Many objects appear variable (about 6% at the 99% significance level), but we decided to focus on those that display a pronounced variability between observations ($\chi^2 \geq 100$) and are bright enough to allow for a detailed analysis of their lightcurve and spectrum. In this way, we have identified eight objects that display a strong flare during one of the observations (see Fig. 6). It should be emphasized that we are not aiming to establish a complete census of variable sources, but to characterize the properties of the brightest flaring candidates. Note that in some cases we find that the observation does not cover the entire flare but only the decay phase.

6.1. Flaring region

The spectra and lightcurves were extracted for the flare observation over circular regions with a radius of at least 1.25 arcsec. For isolated sources, the background was evaluated over a source-free annulus surrounding the source region. However, in the crowded, inner regions of the cluster, we evaluated the background over a circular, source-free, region as close as possible to the source. For the lightcurves, whenever possible, we have determined the $1/e$ decay times of the flares (τ_{obs}) by a least-square fit of the exponential decay (see Table 5). Due to

the limited number of counts, the lightcurves had to be binned into 5 ks bins, thus limiting our ability to determine decay times shorter than this binning time. However, all but one source actually have $\tau_{\text{obs}} > 5$ ks. On the other hand, the spectra were fitted with an absorbed (wabs) single temperature, solar abundance, mekal model. Unfortunately, the sources are still too faint to extract time-resolved spectra over the duration of the flare, and the spectral analysis was therefore done for the whole exposure. The results of the fits are provided in Table 5. The best fit plasma temperatures are all quite high ($kT \geq 2.2$ keV) as expected for pre-main sequence (PMS) stars during a flare. We note that the best-fit column densities are larger than the interstellar column ($\sim 1 \times 10^{22} \text{ cm}^{-2}$) expected from the average reddening towards the massive stars of Westerlund 2.

Correlating the positions of the flaring sources with the 2MASS point-source catalogue ([Cutri et al. 2003](#)), we find that sources A, B, D, and G have a near-IR counterpart within less than one arcsecond. However, the only source with good quality 2MASS photometry is Src A ($J = 15.47$, $H = 14.80$ and $K_s = 14.46$), the other three have highly uncertain measurements.

Assuming that the flaring plasma is confined in a closed, coronal loop as is the case for solar flares, we can use the simple analytical approach proposed by [Serio et al. \(1991\)](#), for an application of the method see e.g. [Favata et al. 2005](#)) to express the loop half-length l as a function of the maximum temperature at the top of the loop T_{max} and the thermodynamic decay time τ_{th}

$$l \sim 0.132 \tau_{\text{th}} \sqrt{kT_{\text{max}}}$$

here l is expressed in R_\odot , kT in keV and τ_{th} in ks. When the temperatures are determined from fits of ACIS CCD spectra, a correction has to be applied to the observed temperature to derive the maximum temperature at the top of the loop ([Favata et al. 2005](#)): $T_{\text{max}} = 0.068 T_{\text{fit}}^{1.20}$ where the temperatures are in K. The observed decay time of the flare exceeds the intrinsic thermodynamical decay time due to the effect of heating that can extend into the decay phase of the flare. The relation between the two, $F(\zeta) = \tau_{\text{obs}}/\tau_{\text{th}}$, can be determined from the slope ζ of the flare decay in a $\log T - \log \sqrt{EM}$ diagram ([Favata et al. 2005](#)). As mentioned above, the flaring sources discussed here are too faint to allow a time-resolved, spectral analysis. Therefore, we can only determine $l \times F(\zeta)$. The corresponding values of $l \times F(\zeta)$ are 3.0–4.8 R_\odot (see Table 5). If we assume that the flaring loops are freely decaying with no heating, $F(\zeta) \simeq 2$ ([Favata et al. 2005](#)); which this represents the lower limit on $F(\zeta)$. Therefore, the typical loop sizes are ≤ 1.5 –2.4 R_\odot . The flaring regions of the PMS stars in Westerlund 2 are compact and typical of many PMS as well as active main-sequence stars that display loops anchored on the stellar photosphere with no interaction with an accretion disk.

6.2. Further evidence for a large distance

[Tsujimoto et al. \(2007\)](#) derived a loose constraint on the distance towards the cluster of 2–5 kpc, based on the median X-ray luminosity of PMS stars in the mass range 2.0–2.7 M_\odot . It appears unlikely that the X-ray data can provide stringent constraints on the distance. If we consider for instance the X-ray luminosity of the flaring sources, we find that their mean, absorption corrected, L_X amounts to $6.7 \times 10^{32} \text{ erg s}^{-1}$ during the flares if we adopt a distance of 8.0 kpc. While this is a high X-ray luminosity, we note that for the brightest flaring sources in NGC 6231, [Sana et al. \(2007\)](#) derived $L_X \sim 3 \times 10^{32} \text{ erg s}^{-1}$. In addition, the

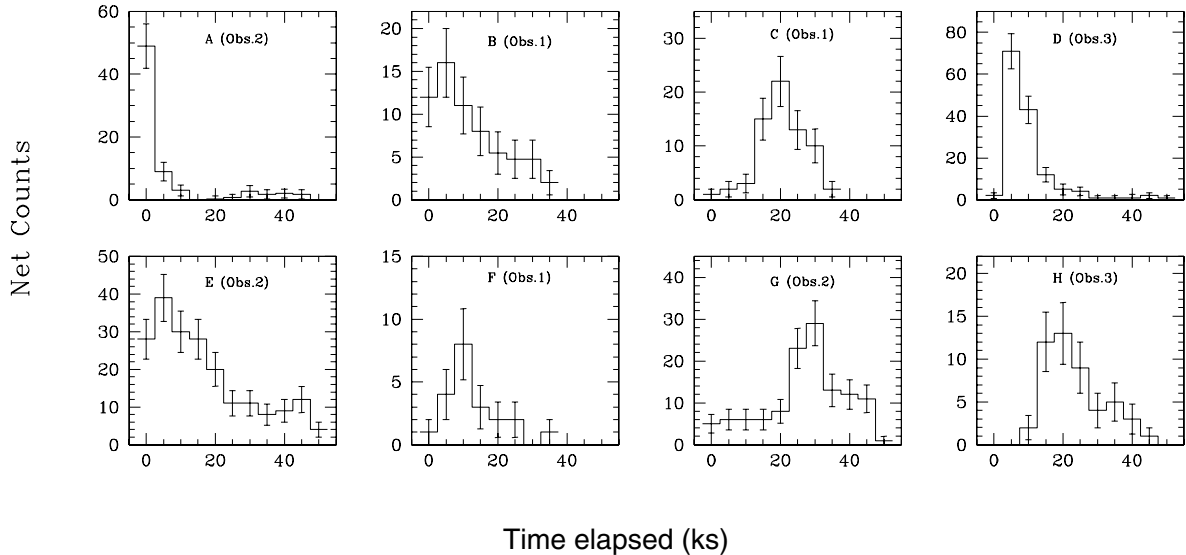


Fig. 6. Light curves of the eight sources that display a strong flare during one of the *Chandra* observations of Westerlund 2. The sources are identified as in Table 5 and the number of the observation where the flare occurred is also indicated. For each panel the *x*-axis shows the time (in ks) elapsed since the beginning of the observation. The lightcurves were binned with a time bin of 5 ks but note that the first and last bins might be affected by incompleteness.

Table 5. Spectral analysis of the flaring PMS candidates, ordered by RA. Columns 2 and 3 yield the coordinates (J2000) of the sources, whilst the fourth column indicates the number of the observation during which the flare occurred. Columns 5–9 list the best fit parameters of the spectral fits with a *wabs × mekal* model. For each parameter, the lower and upper limits of the 90% confidence interval are noted as indices and exponents, respectively. Finally, Col. 10 yields the $1/e$ decay time of the flare; kT_{\max} is the maximum plasma temperature during the flare (derived from the fitted kT) and l is the loop half-length.

Source #	RA	Dec	Obs. #	N^{H} (10^{22} cm^{-2})	kT (keV)	f_X^{abs} ($10^{-14} \text{ erg cm}^{-2} \text{ s}^{-1}$)	f_X^{unabs} ($10^{-14} \text{ erg cm}^{-2} \text{ s}^{-1}$)	χ^2_{ν} (d.o.f.)	τ_{obs} (ks)	kT_{\max} (keV)	$l \times F(\zeta)$ (R_{\odot})
A	10:23:34.27	-57:48:09.3	2	<0.21	$4.05^{9.93}_{2.02}$	1.4	1.4	1.75 (4)	2.4		
B	10:23:57.20	-57:42:59.5	1	$2.39^{4.78}_{1.08}$	$5.24^{79.9}_{1.96}$	8.8	16.1	0.39 (8)	8.7	12.8	4.1
C	10:24:00.00	-57:44:21.5	1	$1.35^{2.11}_{0.84}$	≥ 3.18	4.7	6.2	0.47 (9)	6.6		
D	10:24:00.86	-57:45:56.8	3	$2.07^{2.84}_{1.27}$	$5.93^{42.9}_{3.02}$	5.2	8.9	1.12 (11)	6.2	14.9	3.2
E	10:24:01.58	-57:45:22.7	2	$1.56^{2.19}_{1.07}$	$3.91^{9.41}_{2.30}$	6.0	10.9	0.74 (16)	12.0:	9.0	4.8
F	10:24:02.05	-57:44:33.0	1	$1.37^{0.30}_{5.74}$	> 1.78	2.6	3.4	0.76 (1)			
G	10:24:03.21	-57:45:34.5	2	$1.70^{2.77}_{0.88}$	$3.22^{15.0}_{1.57}$	3.0	6.1	1.66 (8)	10.6	7.2	3.7
H	10:24:10.15	-57:46:35.9	3	$3.00^{5.07}_{1.16}$	$2.17^{9.72}_{0.98}$	1.2	4.2	0.28 (5)	10.7	4.5	3.0

brightest flaring sources in the Orion Nebula Cluster observed by the COUP project display peak luminosities of $8 \times 10^{32} \text{ erg s}^{-1}$ (Favata et al. 2005). The luminosities of our flaring sources in Westerlund 2 are not untypical, especially since they are probably biased towards high values: first, we have selected only the brightest flaring objects; second, these luminosities were corrected for the full column densities derived from the spectral fits. As noted above, these column densities are larger than the values estimated from the interstellar reddening of the early-type stars in the cluster core and our absorption-corrected X-ray fluxes might thus be slightly overestimated.

Our X-ray data might however provide hints for constraining the distance of Westerlund 2. A total of 202 X-ray sources have an optical counterpart within $1''$ of the positions derived using the *BV* photometric data of Rauw et al. (2007) (see Fig. 7). The color-magnitude diagram of these sources indicates that most of the X-ray sources with an optical counterpart appear along the main sequence of the cluster or are foreground field stars. The

latter objects provide a large fraction of the counterparts, a fact apparently underestimated by Tsujimoto et al. (2007). In addition, the color-magnitude diagram shows no sign of the ZAMS turn-on. None of our flaring sources¹⁰ appear to be associated with an optical source in our photometry. The optical counterparts of these sources must be fainter than $V = 21$. For very young clusters such as e.g. NGC6231 (Sana et al. 2007), the optically-brightest PMS stars that display X-ray emission are found to have absolute magnitudes of $M_V \simeq 0.5\text{--}1.5$, in good agreement with the predictions of evolutionary models (Siess et al. 2000). For a distance of 8.0 kpc ($DM = 14.52$) and interstellar extinction $A_V = 4.7\text{--}5.8$ (Rauw et al. 2007), the optically-brightest PMS stars in Westerlund 2 would be expected to occur somewhere in the range $V = 19.7\text{--}21.9$. If the cluster is at 2 kpc, the turn-on would be brighter by 3 mag and would be easily spotted in our data, and counterparts to our sources could be

¹⁰ Note that source A falls outside the field-of-view covered by our photometric data.

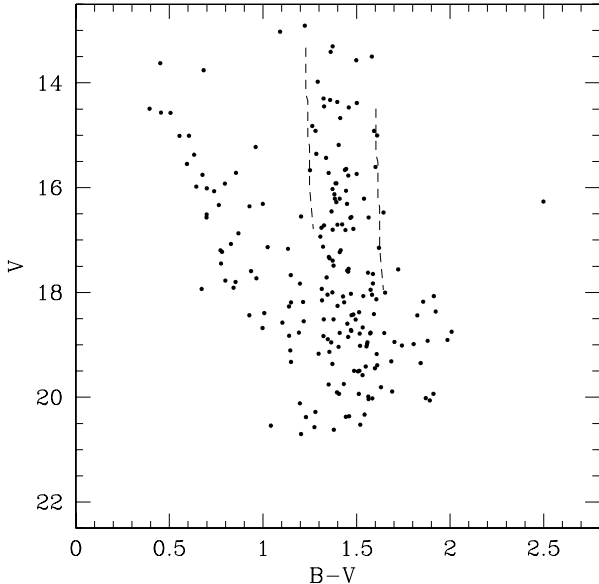


Fig. 7. ($B - V$, V) color-magnitude diagram of the X-ray sources that have an optical counterpart within a correlation radius of less than $1''$. The dashed lines correspond to the main-sequence between spectral types O3 and B2 for a distance modulus of 14.52 and reddened with $A_V = 4.68$ (leftmost curve) or 5.84 (rightmost curve) and assuming $R_V = 3.1$.

detected. Their absence therefore suggests a large distance for the cluster.

7. Conclusion

In this paper, we have analyzed three Chandra observations aimed at monitoring the massive objects of Westerlund 2. In this heavily-obscured region, 24 O-type stars previously identified or candidate were detected and analyzed. Most of these stars display typical values of the L_X/L_{BOL} ratio, although the scatter is rather large (about 60%) due to the low signal-to-noise ratio of the X-ray spectrum, poorer knowledge of the bolometric luminosities and multiplicities. The most X-ray luminous objects (MSP18, 165, 167 and 188) are probably binaries, but further spectroscopic follow-up observations are required for this to be confirmed. About half of the O-type stars also exhibit variability at the 2σ level or more, which is puzzling given their apparent single status.

WR20a, the most massive binary, displays a hard and heavily absorbed X-ray spectrum. It brightens by about 40% in the X-ray domain during the photometric eclipses. The X-ray emission is believed to originate mainly from the wind-wind collision region, which would easily explain the presence of a high temperature in the best-fit models. If the colliding-wind region is sufficiently large and opaque, a modulation will appear when the system rotates and it should then be brighter when seen “face-on”, as is the case during eclipses. The other Wolf-Rayet star of the field, WR20b, is thought to be single and its flux is accordingly constant. However,

the star also exhibits a high temperature and a high X-ray luminosity, and its hardness ratio is even larger than for WR20a. These latter characteristics are more typical of colliding-wind binaries.

The photometry of the other X-ray sources was examined for each observation. Many objects appear variable, and we focused on the eight brightest, flaring ones. Their lightcurve decay time and spectral properties enabled us to infer rather compact flaring regions. The comparison between the optical and X-ray properties of the X-ray sources again suggest a large distance for Westerlund 2.

Acknowledgements. We acknowledge support from the Fonds National de la Recherche Scientifique (Belgium) and the PRODEX XMM and Integral contracts. We also wish to thank Drs. M. De Becker, H. Sana and I. Stevens for their careful reading of the manuscript and their useful comments.

References

- Aharonian, F., Akhperjanian, A. G., Bazer-Bachi, A. R., et al. 2007, *A&A*, 467, 1075
- Anchordoqui, L. A., Beacom, J. F., Butt, Y. M., et al. 2007, in Proc. 30th International Cosmic Ray Conference [[arXiv:0706.0989](#)]
- Antokhin, I. I., Owocki, S. P., & Brown, J. C. 2004, *ApJ*, 611, 434
- Antokhin, I. I., Rauw, G., Vreux, J.-M., van der Hucht, K. A., & Brown, J. C. 2007, *A&A*, in press
- Ascenso, J., Alves, J., Beletsky, Y., & Lago, M. T. V. T. 2007, *A&A*, 466, 137
- Bednarek, W. 2007, *MNRAS*, 382, 367
- Belloni, T., & Mereghetti, S. 1994, *A&A*, 286, 935
- Berghöfer, T. W., Schmitt, J. H. M. M., Danner, R., & Cassinelli, J. P. 1997, *A&A*, 322, 167
- Bohlin, R. C., Savage, B. D., & Drake, J. F. 1978, *ApJ*, 224, 132
- Churchwell, E., & Glimpse, T. 2005, *RMxAC*, 23, 53
- Cutri, R. M., Skrutskie, M. F., Van Dyk, S., et al. 2003, The 2MASS All-Sky Catalog of Point Sources, University of Massachusetts and Infrared Processing and Analysis Center (IPAC/California Institute of Technology)
- Dame, T. M. 2007, *ApJ*, 665, L163
- Favata, F., Flaccomio, E., Reale, F., et al. 2005, *ApJS*, 160, 469
- Gosset, E., Nazé, Y., Claeskens, J.-F., et al. 2005, *A&A*, 429, 685
- Goldwurm, A., Caraveo, P. A., Bignami, G. F., *ApJ*, 322, 349
- Lemaster, M. N., Stone, J. M., & Gardiner, T. A. 2007, *ApJ*, 662, 582
- Martins, F., & Plez, B. 2006, *A&A*, 457, 637
- Martins, F., Schaerer, D., & Hillier, D. J. 2005, *A&A*, 436, 1049
- Moffat, A. F. J., Shara, M. M., & Potter, M. 1991, *AJ*, 102, 642 ([MSP]#)
- Rauw, G., Crowther, P. A., De Becker, M., et al. 2005, *A&A*, 432, 985
- Rauw, G., Manfroid, J., Gosset, E., et al. 2007, *A&A*, 463, 981
- Sana, H., Rauw, G., Nazé, Y., Gosset, E., & Vreux, J.-M. 2006, *MNRAS*, 372, 661
- Sana, H., Rauw, G., Sung, H., Gosset, E., & Vreux, J.-M. 2007, *MNRAS*, 377, 945
- Serio, S., Reale, F., Jakimiec, J., Sylwester, B., & Sylwester, J. 1991, *A&A*, 241, 197
- Siess, L., Dufour, E., & Forestini, M. 2000, *A&A*, 358, 593
- Shara, M. M., Smith, L. F., Potter, M., & Moffat Anthony, F. J. 1991, *AJ*, 102, 716
- Skinner, S. L., Zhekov, S. A., Güdel, M., & Schmutz, W. 2002, *ApJ*, 579, 764
- Stevens, I. R., Blondin, J. M., & Pollock, A. M. T. 1992, *ApJ*, 386, 265
- Townsley, L. K., Feigelson, E. D., Montmerle, Th., et al. 2003, *ApJ*, 593, 874
- Townsley, L., Feigelson, E., Montmerle, T., et al. 2004, in X-ray and Radio Connections, ed. L. O. Sjouwerman, & K. K. Dyer [[arXiv:astro-ph/0406349](#)]
- Tsujimoto, M., Feigelson, E. D., Townsley, L. K., et al. 2007, *ApJ*, 665, 719
- van der Hucht, K. A. 2001, *NewAR*, 45, 135
- Whiteoak, J. B. Z., & Uchida, K. I. 1997, *A&A*, 317, 563